



HAL
open science

Origin and Evolution of Synoptic-Scale Vortices Initiated at Low Level Downwind of the Hoggar Mountains

Jean-Philippe Duvel

► **To cite this version:**

Jean-Philippe Duvel. Origin and Evolution of Synoptic-Scale Vortices Initiated at Low Level Downwind of the Hoggar Mountains. *Monthly Weather Review*, 2023, 151 (7), pp.1631-1645. 10.1175/MWR-D-22-0335.1 . hal-04305728

HAL Id: hal-04305728

<https://hal.sorbonne-universite.fr/hal-04305728v1>

Submitted on 24 Nov 2023

HAL is a multi-disciplinary open access archive for the deposit and dissemination of scientific research documents, whether they are published or not. The documents may come from teaching and research institutions in France or abroad, or from public or private research centers.

L'archive ouverte pluridisciplinaire **HAL**, est destinée au dépôt et à la diffusion de documents scientifiques de niveau recherche, publiés ou non, émanant des établissements d'enseignement et de recherche français ou étrangers, des laboratoires publics ou privés.

Copyright

1 **Origin and evolution of synoptic-scale vortices initiated at low-level**
2 **downwind of the Hoggar Mountains**

3
4
5 Jean-Philippe Duvel

6 *Laboratoire de Météorologie Dynamique, CNRS, Paris, France*

7
8
9
10 Submitted to Monthly Weather Review

11 December 2022

12
13 Revised version: March 2023

14
15
16
17
18
19
20
21 *Corresponding author address:*
22 Laboratoire de Météorologie Dynamique,
23 École Normale Supérieure,
24 24, rue Lhomond, F75231 Paris, France
25 jpduvel@lmd.ipsl.fr
26

27

ABSTRACT

28 Numerous low-level vortices are initiated downwind of the Hoggar Mountains and
29 progress towards the Atlantic coast on the northern path of African Easterly Waves (AEWs).
30 These vortices occur mostly in July and August and more specifically when the northern
31 position of the Saharan heat low (SHL) generates stronger and vertically expanded easterly
32 winds over Hoggar mountains. At synoptic time-scales, a composite analysis reveals that
33 vortex initiation and westward motion are also statistically triggered by a reinforcement of
34 these easterly winds by a wide and persistent high-pressure anomaly developing around the
35 Strait of Gibraltar and by a weak wave trough approaching from the east. The vortices are
36 generated in the lee of the Hoggar, about 1000 km west of this approaching trough, and
37 intensify rapidly. The evolution of the vortex perturbation is afterward comparable with the
38 known evolution of the AEWs of the northern path and suggest a growth due to dry
39 barotropic and baroclinic processes induced in particular by the strong cyclonic shear
40 between the reinforced easterly winds and the monsoon flow. These results show that vortex
41 genesis promoted by changes in orographic forcing due to the strengthening of easterly winds
42 over Hoggar mountains is a source of intensification of the northern path of AEWs in July
43 and August. These results also provide a possible mechanism to explain the role of the SHL
44 and of particular mid-latitude intraseasonal disturbances on the intensity of these waves.

45 **1. Introduction**

46 Over West Africa, synoptic-scale vortices associated with the trough of African Easterly
47 Waves (AEWs) are moving on two paths located roughly on either side of 15°N. Vortices on
48 the northern path are dry and located mostly at low-level (i.e. ~850hPa), while vortices on the
49 southern path are associated with deep convection and located mostly at mid-level (i.e.
50 ~700hPa) near the African Easterly Jet (AEJ) (see e.g., Thorncroft and Hodges 2001, Chen et
51 al. 2008, Hopsch et al. 2007, Duvel 2021). The initiation of a vortex at a given pressure level
52 corresponds to a deepening of the wave trough and therefore to an intensification of the
53 AEW. This deepening will sometimes persist for long distances over West Africa and the
54 Atlantic Ocean where vortices of both paths are known sources of tropical storms and
55 hurricanes (see e.g., Hopsch et al. 2007, Chen et al. 2008, Chen and Liu 2014, Russel et al.
56 2017, Duvel 2021). In July and August, low-level vortices on the northern path are initiated
57 mostly over a small region in the lee of Hoggar mountains Duvel (2021). The objective of
58 this paper is to explore the conditions of formation of these “Hoggar vortices”, in relation to

59 seasonal and intraseasonal variations of the atmospheric circulation over the Hoggar
60 orography.

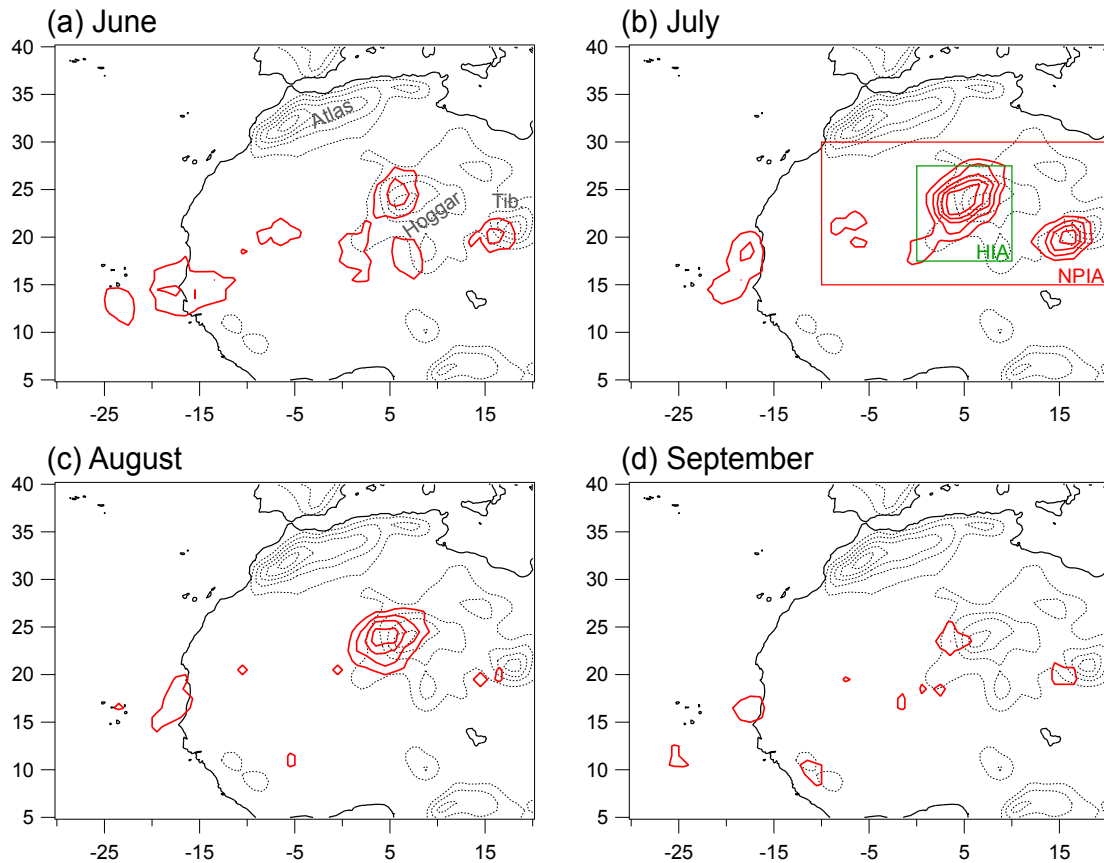
61 The role of orography in triggering or intensifying AEW on the northern (hereafter AEW-
62 N) or the southern (AEW-S) path has been proposed by many studies since pioneer work
63 based on radiosonde measurements. Carlson (1969) first suggested that the origin of AEW-S
64 could be linked to moist convection over the topography of central and eastern Africa. This
65 role of orographic convection has been later established in more detail by several studies
66 using meteorological analyzes and satellite measurements (Reed et al. 1988, Thorncroft and
67 Hodges 2001, Berry and Thorncroft 2005, Mekonnen et al. 2006, Mekonnen and Rossow
68 2018). Dry orographic processes were also mentioned, like in Reed et al. (1988) who
69 identified a cluster of AEW-N initiations located over the Sahara downwind of the Hoggar
70 Mountains ($\sim 5^{\circ}\text{E}$, 24°N). Thorncroft and Hodges (2001) also found more frequent low-level
71 vortex initiation downstream of the Hoggar Mountains and invoked the possible role of
72 orography in the genesis of the low-level northern path disturbances. Duvel (2021) found that
73 most of the low-level AEW-N vortices that reach the Atlantic Ocean, where they may trigger
74 tropical cyclones, are initiated just west of the Hoggar Mountains in July and August. In
75 addition to their potential role in cyclogenesis, Fiedler et al. (2014) found many of these low-
76 level cyclonic disturbances are at the origin of Saharan dust lifting between the Hoggar and
77 the Atlantic Ocean.

78 Studies based on numerical model simulations also suggested that the interaction between
79 the Hoggar mountains and the large-scale flow could impact AEW-N. Thorncroft and Rowell
80 (1998) showed that the strength of the low-level northeasterly flow over the Hoggar impact
81 AEW-N amplitude. Hamilton et al. (2020) showed that the wave kinetic energy at low-level
82 is reduced north of 15°N over West Africa when the topography is reduced or removed.
83 White et al. (2021) showed more specifically a large reduction of the kinetic energy of AEW-
84 N when the Hoggar and Tibesti Mountains are removed, due to reduction in baroclinic energy
85 conversion related to reduced vertical wind shear. The initiation of vortices by a dry flow
86 around a mountain was studied in Mozer and Zehnder (1996a, b) using an idealized
87 numerical model. They showed that the blocking of an easterly flow by the Hoggar mountain
88 may generate a barotropically unstable jet at low level which produces lee vortices
89 downstream, being a possible source of AEW-N. Smaller meso-scale vortices are also
90 initiated in the cyclonically sheared strip between the Harmattan and the monsoon flow. For

91 example, Bou Karam et al. (2009) studied short-lived and stationary vortices of smaller sizes
92 initiated south of the Hoggar Mountains.

93 Previous studies have therefore suggested that the orographic forcing of the Hoggar plays
94 a role in the initiation or intensification of AEW-N. In contrast with AEW-S, the deep
95 convection must have little direct influence on wave initiation and growth for AEW-N path
96 that is located north of 15°N over the Sahara Desert. Moreover, the AEW-N path is located
97 more than 10° north of the AEJ core and near the surface, suggesting that physical sources
98 other than AEJ instabilities may play a significant role on AEW-N activity. The literature
99 review above shows that few papers have specifically addressed the observed seasonal and
100 intraseasonal mechanisms behind the initiation of vortices downwind of the Hoggar and the
101 impact of these vortices on AEW-N activity. These papers are based either on idealized
102 simulations (Mozer and Zehnder, 1996b) or on sensitivity studies using numerical models
103 with or without orography (see e.g., Hamilton et al. 2020, White et al. 2021). These
104 sensitivity studies provide an estimate of the overall impact of orography on AEW-N, but as
105 the removal of orography also significantly affects the mean dynamics and thermodynamics,
106 it is difficult to isolate the specific orography processes that play a role in the AEW-N
107 dynamics.

108 The objective of this paper is to study the origin of the observed initiation of low-level
109 vortices in the lee of the Hoggar by relating this initiation to characteristics of the large-scale
110 flow over this mountain. This paper considers two time-scales, the seasonal time scale to
111 explore the average large-scale conditions that may explain why the Hoggar vortices are
112 mostly initiated in July and August and the synoptic time scales that gives the particular
113 conditions at time of vortex initiation. Section 2 presents the analysis approach and gives a
114 statistic on the vortex tracks and on their impact on the AEW-N signal. The origin of the
115 seasonal variation of the circulation over the Hoggar and its potential effect on vortex
116 initiation and propagation is discussed in section 3. The conditions of formation of the
117 vortices at synoptic time-scales (i.e. 2-10 days) are presented in section 4 and the
118 characteristics of the vortices as they move toward the African coast are presented in section
119 5. The impact of these results on the origin of AEW-N is discussed in section 6.



120
 121 Figure 1: **(red contours)** Number of primary “Atlantic Vortex” initiations for a given month in 1° boxes for the
 122 38 years. For a better legibility, initiation fields are smoothed by a 3°x3° running mean. The first contour is 0.5
 123 and the contour increment is 0.5. **(black dotted contours)** Orography with a contours every 250m from 500m.
 124 On panel b, the red rectangle defines the North Path Initiation Area (NPIA) for initiation of AEW-N vortices, the
 125 green square defines the Hoggar Initiation Area (HIA) for “Hoggar vortices”

126 2. Analysis approaches and vortex statistics

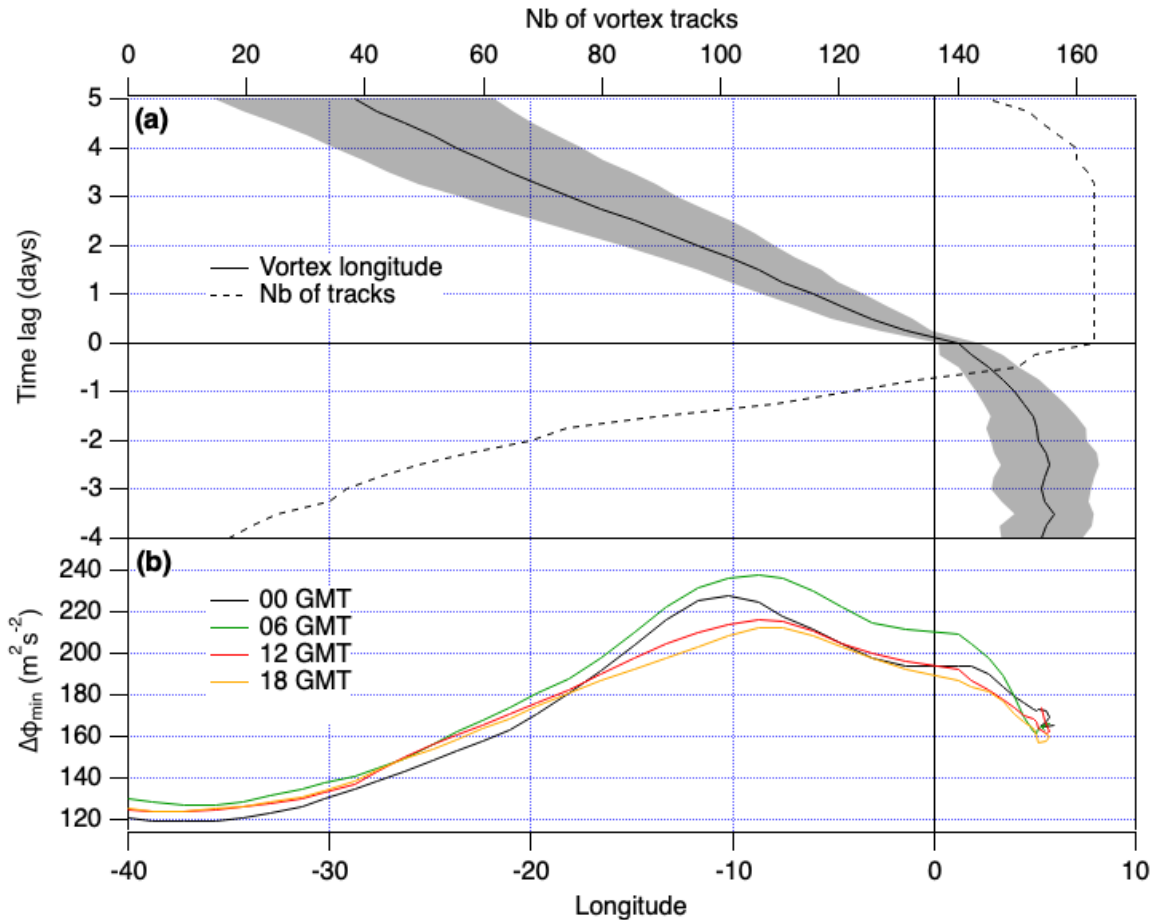
127 *Vortex tracking algorithm*

128 The analysis is based on ERA-Interim (Dee et al. 2011) meteorological re-analyses
 129 between 1980 and 2017 with a horizontal resolution of 0.75° x 0.75° and a 6-hour time step.
 130 In order to assess the proper representation of the vortices in ERA-I and to analyze possible
 131 impact of these vortices on the cloudiness, we also use brightness temperatures of the
 132 CLAUS (Cloud Archive User Service) dataset (Hodges et al., 2000) that are available with a
 133 3-hour time step for years 1983 to 2009. The set of vortex tracks used in this study is the
 134 same as that used in Duvel (2021) and is obtained using the objective tracking approach
 135 described in Duvel (2015) and Duvel et al. (2017). This approach is based on geopotential
 136 height anomaly $\Delta\phi$ for a particular isobar (850 hPa here for AEW-N vortices). At a given
 137 grid point, $\Delta\phi$ is defined as the difference between the geopotential height and its average

138 over a region of $\pm 7.5^\circ$ (i.e., ± 10 ERA-I gridpoints) centered on the grid point. The “vortex
139 area” is an ensemble of continuous model grid points with values of $\Delta\phi$ lower than a negative
140 threshold. This threshold is adjusted for each vortex and each time step to limit the vortex
141 size to a maximum area of 100 model grid points (i.e., a radius of 4.2° for a circular shape).
142 The intensity of a vortex is given by the minimum value $\Delta\phi_{min}$ (i.e., maximum absolute
143 value) of $\Delta\phi$ in the vortex area. A given vortex is tracked over time by considering the
144 overlap between the vortex areas for two consecutive time steps. A vortex track is therefore a
145 time series of the successive position of the barycenter (i.e. the center weighted by $\Delta\phi$) of
146 these vortex areas, the first position being considered as the initiation location. As in Duvel
147 (2021), we only consider vortex tracks that last more than two days and remain at least one
148 day over the Atlantic Ocean. These vortices are called “Atlantic vortices” hereinafter. For the
149 “Atlantic vortex” distribution maps reported in Figure 1, we consider only primary vortex
150 initiations at 850 hPa. A primary initiation corresponds to a first vortex detection that does
151 not result from the vertical extension on an already existing vortex track at another pressure
152 level (700 hPa here). This distinction is mostly useful for the AEW-S path and near the coast
153 where many low-level initiations are related to downward extension of mid-level vortices
154 (Duvel 2021). The area of initiation of AEW-N vortices is defined as the area north of 15°N
155 and east of 10°W , which is the Northern Path Initiation Area (NPIA) outlined in red in Figure
156 1b. Over the NPIA, most low-level AEW-N vortices initiations are primary initiations
157 (Duvel, 2021) and this distinction is therefore not made in what follows. A vortex track is
158 considered cyclogenetic if it is located within 3° of an IBTrACS system (Knapp et al. 2010)
159 for at least one time step.

160 *Atlantic Vortex initiation statistics*

161 Between June and September, there are about 3 Atlantic vortices initiated each month at
162 850 hPa over the NPIA and about 12% of these vortices are cyclogenetic (Table 1). There is
163 also a large seasonal variation of the number of initiations, with a maximum of 4.4 per month
164 in July and less than 2 per month in September. The cyclogenetic efficiency of these vortices
165 (i.e., the probability that their track matches an IBTrACS system) has a sharp maximum of
166 29% in August. As discussed in Duvel (2021) the cyclogenesis efficiency of these dry AEW-
167 N vortices is indeed as large as the AEW-S vortices in August when the cyclogenesis
168 potential index of the Atlantic Ocean is a maximum. The cyclogenesis efficiency of AEW-N
169 vortices is small on the average because they peak in July when this index is smaller.



170 Figure 2: (a) Average (solid) and standard deviation (gray part) of the Hoggar vortex longitude (bottom axis) as
 171 a function of the time lag in regard to the crossing of the Greenwich meridian for vortex initiated in the main
 172 development region (0°E to 10°E; 17.5°N to 27.5°N) in July and August; (dashed) Number of vortex tracks (top
 173 axis) considered for the different time lags. (b) Corresponding longitudinal distribution of the average absolute
 174 value of $\Delta\phi_{min}$ for four hours of the day.
 175

176 This paper focuses on Atlantic vortices initiated in the Hoggar Initiation Area (HIA: 0°E
 177 to 10°E; 17.5°N to 27.5°N; green square in Fig. 1b). These vortices are hereafter called
 178 "Hoggar vortices". For the 38 years, there are 166 Hoggar vortices that represent more than
 179 60% of the Atlantic vortices of the AEW-N path in July and August. These Hoggar vortices
 180 have a cyclogenetic efficiency comparable to that of all Atlantic Vortices of the AEW-N path
 181 (Table 1).

	(NPIA) North Path Vortices		(HIA) Hoggar Vortices	
	Nb. Initiations	Cyclogenetic	Nb. Initiations	Cyclogenetic
June	2.7	1%	1.2	2%
July	4.4	5%	2.4	2%
August	3.4	29%	1.9	29%
September	1.9	15%	0.6	13%
Average	3.1	12%	1.5	12%

182 Table 1: Monthly average number of initiations (over 1980-2017) and average cyclogenetic probability of
 183 Atlantic vortices of the north path initiated in the NPIA and in the HIA. Seasonal maxima are highlighted in
 184 bold.

185 Figure 2 represents the average longitude and strength attained by the Hoggar vortices at
186 different time lags after they cross the Greenwich meridian. Hoggar vortices move westward
187 with an average speed of about 7.5 ms^{-1} . The beginning of their westward progression is
188 associated with a strengthening of the vortex, as revealed by the increasing absolute value of
189 $\Delta\phi_{min}$ before the passage on the Greenwich meridian (Fig.2b). Before that, due to the
190 persistent depression in the lee of the Hoggar, many vortices first detected by the tracking
191 algorithm in the HIA remain motionless and weak for a variable number of days (Fig.2a). In
192 the following, only diurnal averages will be considered, but it is worth noting that there is a
193 diurnal variation of the dynamic and thermodynamic structure of the boundary layer over
194 West Africa (Parker et al. 2005, Abdou et al. 2010). This is due to the weak turbulent mixing
195 in the boundary layer during nighttime that decreases the effect of the surface friction and
196 generates a low-level vertical stratification. This favors the development of nighttime low-
197 level jets that are maximal at sunrise and that may impact Hoggar vortex intensity. This
198 diurnal cycle has indeed a consistent signature on the vortex intensity over continental
199 regions with maximum absolute value of $\Delta\phi_{min}$ at 0600 GMT and minimum at 1800 GMT
200 (Fig.2b).

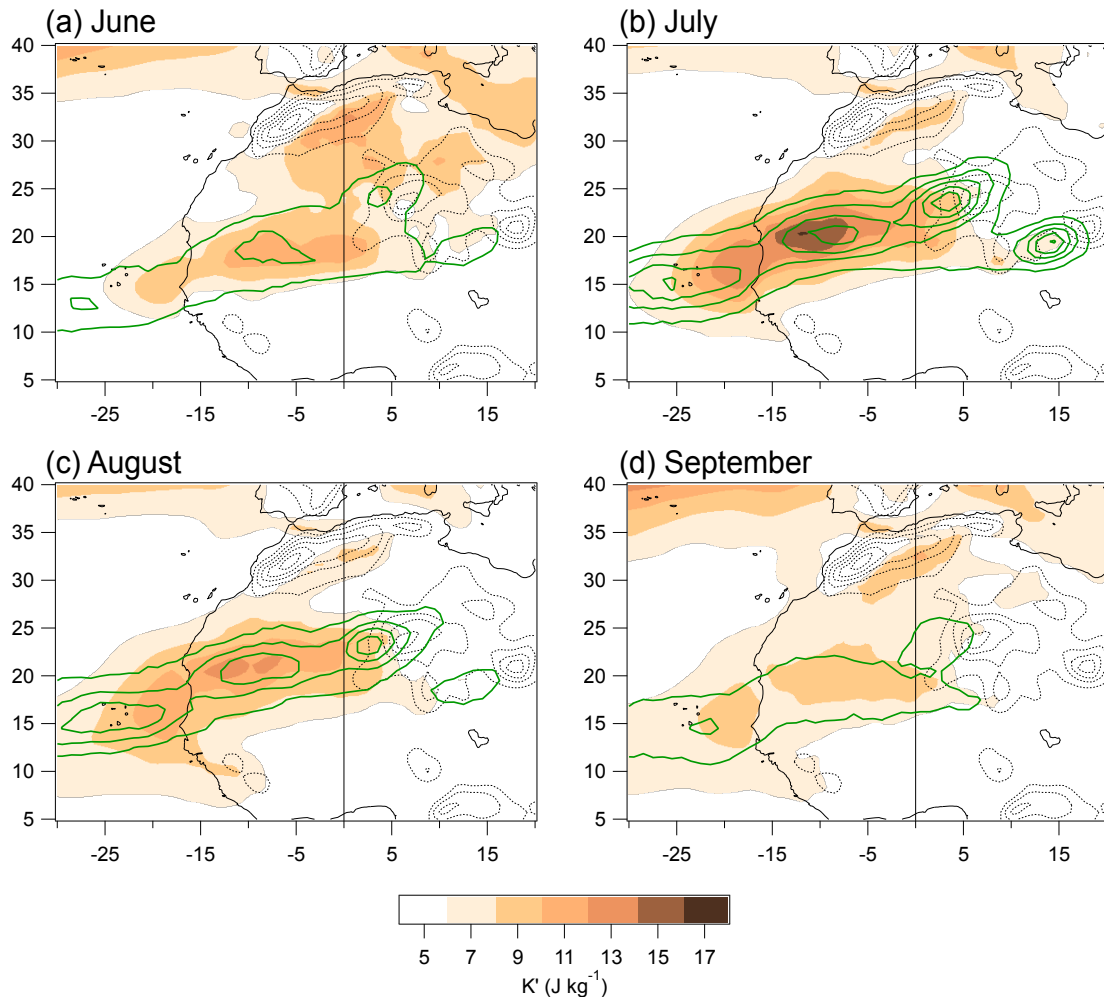
201 *Atlantic Vortex Occurrence and AEW-N amplitude*

202 The AEW-N vortex occurrence, i.e. the number of hours during which a vortex
203 barycenter is present in a given area, is reported in Figure 3. These maps reveal the most
204 probable trajectory of the low-level Atlantic vortices of the north path and show the
205 predominance of vortices initiated near the Hoggar and the Tibesti in July and August. These
206 vortices propagate southwestward to the Atlantic Ocean roughly along the cyclonically
207 sheared strip between the Harmattan wind and the monsoon flow. The relation between
208 Atlantic Vortices and the AEW-N is studied by comparing the vortex occurrence to the
209 AEW-N activity. This activity may be estimated by computing the perturbation kinetic
210 energy K' (in J kg^{-1}) of the horizontal wind at low-level (see e.g., Rydbeck and Maloney
211 2014, Hamilton et al. 2020, White et al. 2021):

$$215 \quad K' = \frac{1}{2}(u'^2 + v'^2) \quad (1)$$

212 where u' and v' are the 2-10-day band-filtered zonal and meridional winds at 850hPa. The
213 distribution of K' shows that regions of high AEW amplitude are also region of large vortex
214 occurrence (Fig.3). In addition, the seasonal variation of K' is also in phase with that of the

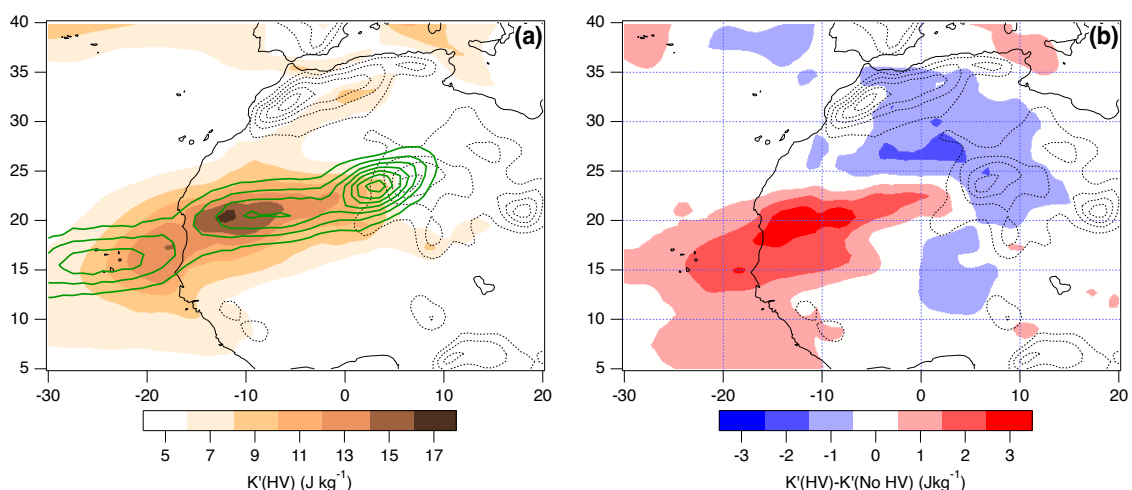
216 vortex occurrence with maximum values in July. The maximum value of K' in July and
 217 August (Fig.3b and 3c) is obtained around 10°W , that is consistent with the longitude of
 218 maximum vortex intensity reported in figure 2b. Over the Atlantic, the decrease in K' despite
 219 the large vortex occurrence is due to the regular weakening of the average vortex amplitude
 220 as they move westward over the Atlantic (Fig.2b).



221
 222 Figure 3: **(green contours)** Occurrence of AEW-N vortices initiated over the NPIA, expressed as the number of
 223 hours by month a vortex barycenter is present in a 1° box. For a better legibility, occurrence fields are
 224 smoothed by a $3^\circ \times 3^\circ$ running mean. The first contour is 0.5 and the contour increment is 1. **(colors)** Monthly
 225 average of the perturbation kinetic energy K' (Eq.1) (J kg^{-1}) of the horizontal wind at 850 hPa in the 2–10-day
 226 band. **(dotted black contours)** Orography with a contours every 250m from 500m.

227 The specific role of the Hoggar vortices on the AEW-N activity is estimated by
 228 comparing K' for periods with (HV) and without (No HV) active Hoggar vortices. Active
 229 Hoggar vortex periods are defined as all time-steps between d_0-1 day and d_0+4 days, d_0 being
 230 the ensemble of days at which each of the 166 Hoggar vortices crosses the Greenwich
 231 meridian. Active Hoggar vortex periods represent about 1/3 of the time for July and August.
 232 As for the average K' , the distribution of K' (HV) for these active periods well corresponds to

233 the specific Hoggar vortex occurrence in July and August (Fig.4a). Compared to K' (No HV),
 234 K' (HV) is augmented by about 20% over the most active region around 20°N and 10°W
 235 (Fig.4b). This confirms that active Hoggar vortex periods correspond to enhanced AEW-N
 236 activity over West Africa. In contrast, K' (HV) is slightly reduced between Hoggar and Atlas
 237 Mountains around 27.5°N, possibly due to the relation between Hoggar vortex initiations and
 238 relatively stable (and thus giving smaller K') northeasterly winds associated with
 239 intraseasonal mid-latitudes perturbations (see section 4). Note that adding vortices initiated
 240 downwind of the Tibesti mountains (those around 20°N-15°E in Fig.1b), about 220 vortices
 241 cross the Greenwich meridian and K' (HV) is reinforced by about 30% around 20°N and
 242 10°W compared to K' (No HV) (not shown). This highlights the fact that the impact of
 243 vortices initiated near the orography on the AEW amplitude is broader than the impact of the
 244 Hoggar vortices alone. Nevertheless, as the conditions of vortex initiation over the Tibesti
 245 and the Hoggar are slightly different, the following analyses will focus on Hoggar vortices
 246 only.

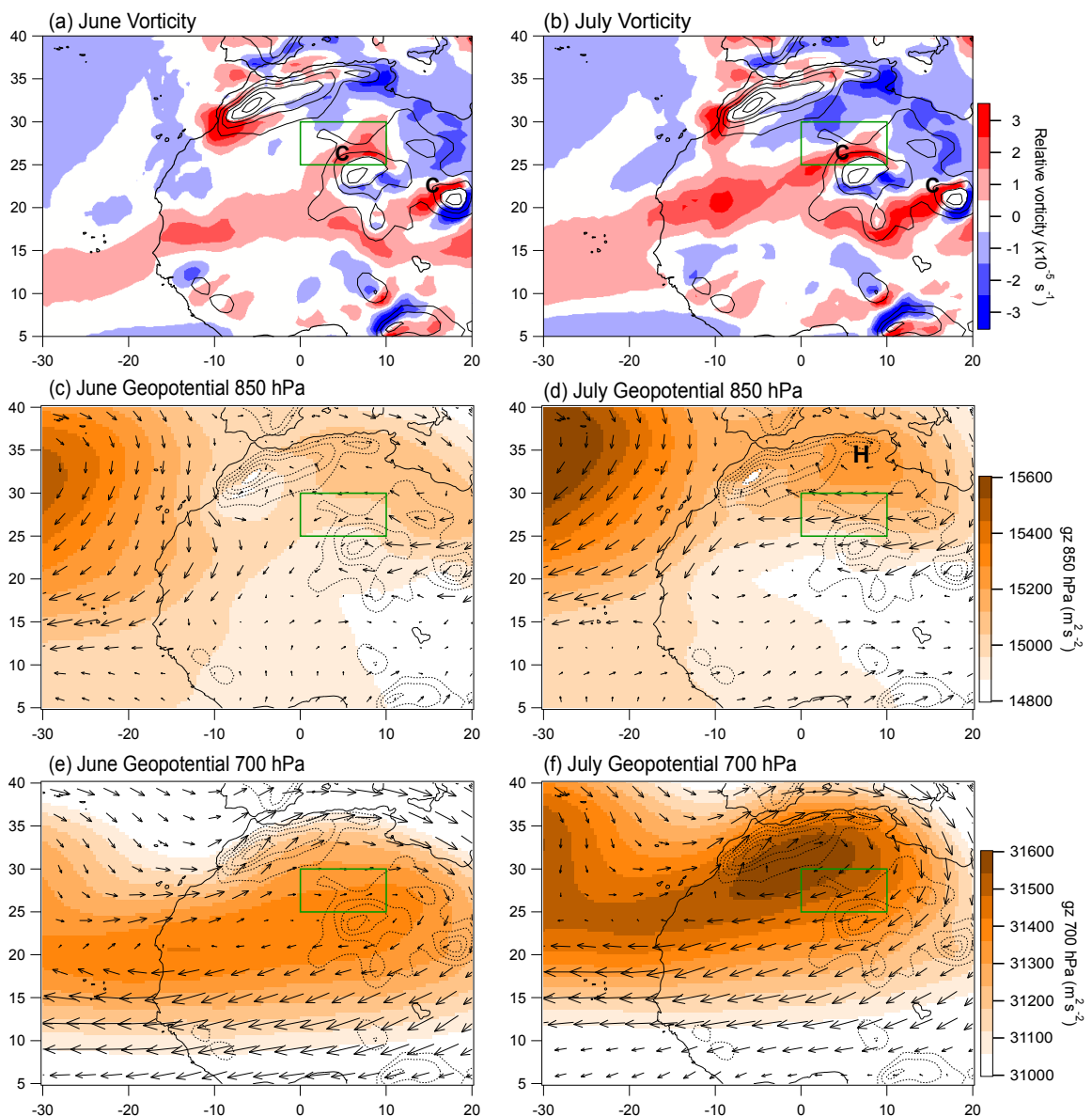


247 Figure 4: (a) (colors) Average perturbation kinetic energy K' (J kg^{-1}) of the horizontal wind at 850 hPa in the 2-
 248 10-day band in July and August for periods with active Hoggar vortices. (green contours) Occurrence of
 249 “Hoggar Vortices” initiated in the HIA, expressed as the number of hours a vortex barycenter is present in a 1°
 250 box. For a better legibility, occurrence fields are smoothed by a $3^\circ \times 3^\circ$ running mean. The first contour is 1 and
 251 the contour increment is 1. (b) (colors) Average K' difference between periods with (HV) and without (No HV)
 252 Hoggar vortices. All differences in red or blue are significant at more than 99%. (dotted black contours)
 253 Orography with a contours every 250m from 500m.
 254

255 *Composite analysis*

256 In section 4, synoptic time-scale perturbations corresponding to Hoggar vortex initiation
 257 are studied using a composite analysis. The reference days d_0 of the composite are days when
 258 the barycenter of a Hoggar vortex crosses the Greenwich meridian. This meridian is the
 259 western boundary of the HIA and is crossed by Hoggar vortices while they strengthen and

260 begin their progression toward the coast (Fig. 2). This is therefore the relevant criteria to
 261 define the reference day d_0 of the Hoggar vortex composites. Composite fields are computed
 262 by averaging anomalies over the ensemble of days d_0 . Anomalies of a given ERA-I field for
 263 each d_0 is computed as a difference between the daily mean field (4 timesteps beginning at 0
 264 GMT) and a climatological value for this day of the year. This daily climatological value is
 265 obtained by linear interpolation between two monthly averages attributed to the 15th day of
 266 each month. The evolution of the average atmospheric state prior and after Hoggar vortex
 267 initiations is computed following the same procedure between d_0-4 days and d_0+4 days.



268
 269 Figure 5: Average fields for June and July for: (a and b) Average relative vorticity at 900 hPa; (c and d) Average
 270 geopotential height and wind at 850hPa; arrows length is 4° for a wind of 10ms^{-1} ; and (e and f) idem at 700
 271 hPa. (black dotted contours) Orography with a contours every 250m from 500m. The region used in Figure 6 is
 272 highlighted in green.

273

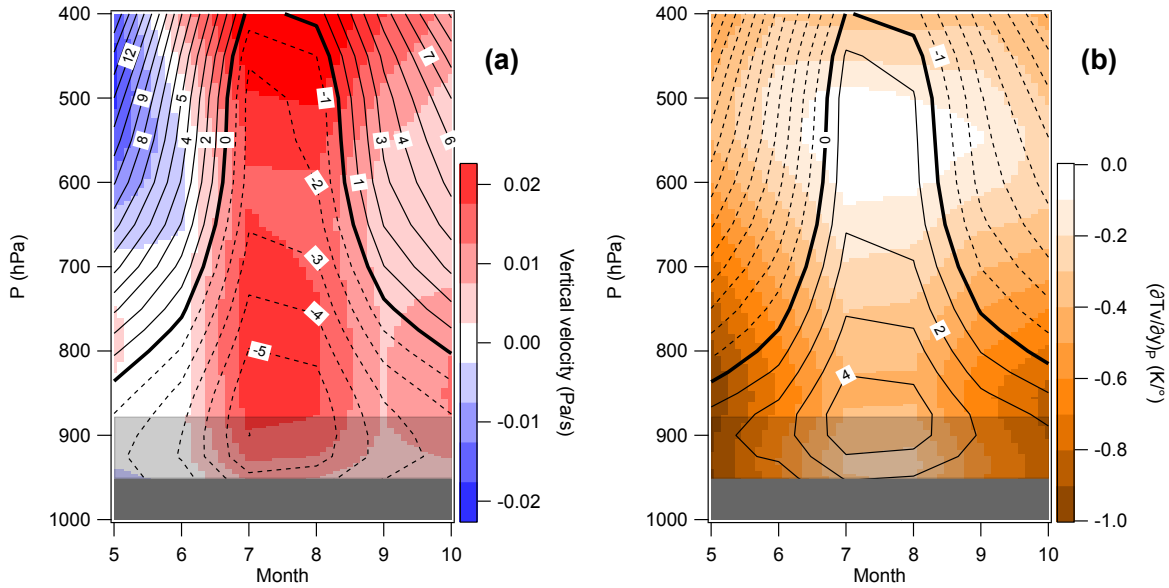
274

275 **3. Seasonal evolution of the large-scale environment**

276 The objective of this section is to extract specificities of the large-scale circulation in July and
277 August and to understand how they can favor vortex initiation in the lee side of the Hoggar
278 mountains. As shown by Sultan and Janicot (2003), there is a sudden onset of the monsoon at
279 the end of June due to the migration of Saharan Heat Low (SHL) and to different positive
280 feedbacks partly linked to orography (Semazzi and Sun 1997). The resulting difference
281 between June and July in low-level wind and vorticity (Fig. 5) reveals two important features
282 that potentially have a significant impact on the increased frequency of Hoggar vortices in
283 July. The first feature is the cyclonic vorticity north of Hoggar and Tibesti mountains (points
284 C in Fig.5) which may be attributed to increased drag closer to the mountain that generates a
285 cyclonic shear in the flow having the mountain to its left. This cyclonic vorticity is larger and
286 extends further west in July. The second feature is the cyclonic strip between the Hoggar and
287 the Atlantic coast due to the horizontal shear between the Harmattan and the monsoon flow.
288 This cyclonic strip is stronger and displaced northward in July in good agreement with the
289 AEW-N activity and vortex occurrence (Fig.3a and 3b). Note that part of the increase in
290 mean vorticity, particularly near 10°W-20°N, must be due to the higher frequency of the
291 vortex itself, but the increase in cyclonic shear is also due to the strengthening of the
292 Harmattan and of the monsoon flow. These two points lead to a continuous and reinforced
293 cyclonic strip between the leeward side of the Hoggar and the coast in July.

294 The development of this strong and continuous cyclonic strip in July is mostly due to the
295 reinforcement of the low-level easterly circulation north of 20°N in association with the
296 reinforced latitudinal pressure gradient at low-level (Fig.5c and 5d). Note that the
297 reinforcement of the anticyclonic circulation of the Libyan High (Point H in Fig.5d) may be
298 favored by orographic effect due to the northeastern edge of Atlas Mountains (Fig.5b). At
299 higher levels, the high pressure generated mostly by the presence of the SHL is centered on
300 the Hoggar in June, giving westerly winds to the northern side of the Hoggar, and reinforced
301 and centered south of the Atlas in July, giving strong easterly winds to the northern side of
302 the Hoggar (Fig.5e and 5f). The seasonal evolution of the zonal wind profiles north of the

303 Hoggar (0°E-10°E; 25°N-30°N; green rectangle in Figure 5) between May and October
 304 shows a clear reinforcement and a vertical extension of easterly winds from the surface up to



305
 306 Figure 6: Evolution of monthly mean profiles for the region (0°E to 10°E; 25°N to 30°N; green region in Figure 5)
 307 between May and October for: (a) the zonal wind (contours, ms⁻¹) and vertical motion (colors in Pa s⁻¹,
 308 positive values for downward motion); (b) latitudinal gradient of the geopotential height (contours, m/°) and
 309 latitudinal gradient of the virtual temperature (colors in K/°). Maximum and average orography for the region
 310 is shown in light and dark grey respectively.

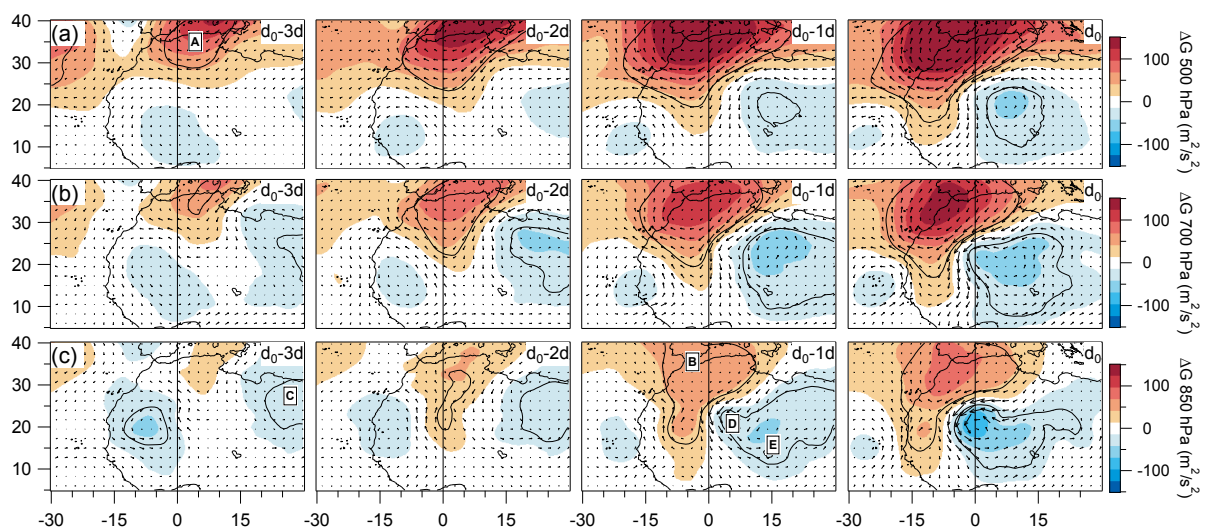
311 400 hPa in July and August, associated with reinforced subsidence (Fig.6a). This can be
 312 mostly attributed to the northward migration of the SHL that places the area north of the
 313 Hoggar under the southeastern descending branch of the Libyan High. Figure 6b shows that
 314 this can be also understood in term of local thermal wind structure for which the zonal
 315 geostrophic wind U_g on an isobar P_n is given by:

$$325 \quad U_g(P_n) = -\frac{1}{f} \left(\frac{\partial \Phi(P_0)}{\partial y} \right)_P - \frac{R}{f} \sum_{i=1}^n \left(\frac{\partial \overline{T_{vi}}}{\partial y} \right)_P \ln(P_{i-1}/P_i) \quad (2)$$

316 where f is the Coriolis parameter, $\phi(P_n)$ the geopotential height of the isobar P_n , $\overline{T_{vi}}$ is the
 317 average virtual temperature between the two pressure levels P_i and P_{i-1} , and R the gas
 318 constant for dry air. Figure 6b is computed using monthly means T_v and $\phi(P_0)$ taken in ERA-
 319 I. The stronger easterly wind near the surface in July is due to larger low-level latitudinal
 320 pressure gradient (first RHS term of Eq.2; contours in Fig.6b) between the Hoggar and the
 321 Mediterranean Sea (Fig.5c and d) that mostly results from the northward migration of the
 322 SHL, as described in Sultan and Janicot (2003). Second, this northward migration of the SHL
 323 reduces the magnitude of the latitudinal gradient of the virtual temperature (second RHS term
 324 of Eq.2; colors in Fig.6b) in July and August and maintains these easterlies up to 400 hPa.

326 Before July and after August, when the SHL is shifted southward, the larger absolute value of
 327 this gradient causes the easterlies to weaken and turn west rapidly with height.

328 In summary, this section shows that the stronger easterly winds over the Hoggar in July
 329 reinforce cyclonic vorticity north and west of the orography and could be at the origin of
 330 more frequent Hoggar vortex initiation during these months. In addition, the northward
 331 displacement and the strengthening of the cyclonic strip between the Hoggar and the coast in
 332 July may promote the development and maintenance of the vortex disturbance through
 333 barotropic and baroclinic processes, as shown by previous analyses of the energy source of
 334 AEW-N (see e.g., Norquist et al. 1977, Diedhiou et al. 2002, and section 5).

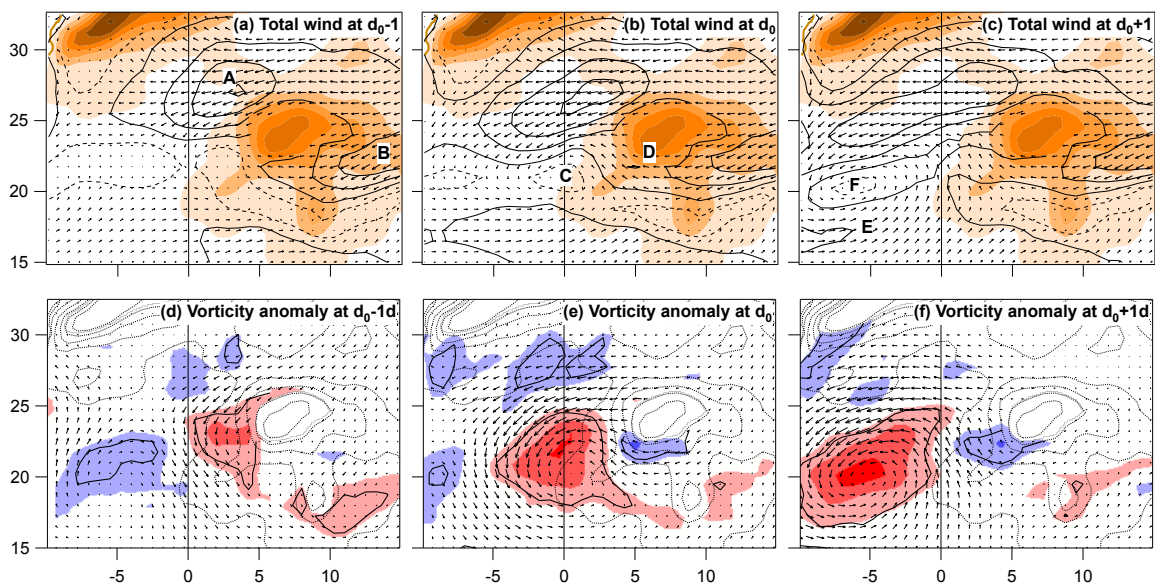


335
 336 Figure 7: Composite of the horizontal wind anomaly (arrows, length of 5° for 5ms^{-1}) and of the geopotential
 337 height anomaly at (a) 500 hPa, (b) 700 hPa and (c) 850 hPa for the period $[d_0 - 3 \text{ days}, d_0]$. The day d_0 is the day
 338 when the barycenter of the Hoggar vortex at 850 hPa crosses the Greenwich meridian. The black contour
 339 delineates regions for which the composite geopotential perturbation is significant at the 99% level.

340 4. Hoggar vortex genesis

341 The objective of this section is to determine large-scale and local conditions leading to
 342 Hoggar vortex initiations. To this end, composites of the 166 Hoggar vortices are computed
 343 for the dates of initiation d_0 and for each of the three days before and after d_0 (see section 2).
 344 Three days before Hoggar vortex initiation, there is a high-pressure anomaly significant at the
 345 99% level above 700 hPa over a region centered near the Strait of Gibraltar (point A in
 346 Fig. 7a). This anomaly amplifies, extends downward and spread horizontally, giving
 347 northeasterly winds blowing at 850 hPa over the Hoggar one day before d_0 . A weak but
 348 statistically significant depression anomaly is also initiated at low-levels three days before d_0
 349 near the Mediterranean Sea around 30°N and 30°E (point C in Fig. 7c). The following days,
 350 this “easterly low” moves westward, extends up to 500 hPa, strengthens and contributes to

351 increase the northeasterly flow over the Hoggar. At d_0-1d , a secondary minimum in the 850
 352 hPa geopotential height anomaly appears in the lee side of the Hoggar (point D in Fig.7c)
 353 more than 1000 km west of the “easterly low” which is still centered at $20^\circ\text{N}-15^\circ\text{W}$ and
 354 shifted southward compared to previous days (point E in Fig.7c). The secondary minimum
 355 may be considered as the initiation of the Hoggar vortex which then strongly intensifies
 356 between d_0-1d and d_0 in association with a horizontal expansion and a strengthening of the
 357 “Gibraltar high”. At d_0 , the vortex is centered on the Greenwich meridian and therefore at 10°
 358 west of the “easterly low” at 500hPa which continues its slow westward progression.



359
 360 Figure 8: (a, b, c) Composite of the total wind field at 900 hPa at d_0-1 day, d_0 , and d_0+1 day. Arrows length is 1°
 361 for 10ms^{-1} and black contours are the wind strength (dotted line for 2ms^{-1} and increment of 2ms^{-1}). (d, e, f)
 362 Composites of relative vorticity (colors as for Fig.5, black contour for statistical significance at 99%) and wind
 363 (arrows length is 1° for 5ms^{-1}) anomalies at 900 hPa. The orography with a height step of 200m is represented
 364 by colors for a, b and c and by dotted contours for d, e, and f.

365 Figure 8 highlights the low-level wind and vorticity evolution near the Hoggar at higher
 366 spatial resolution during vortex initiation. The wind speed is stronger northwest of the
 367 Hoggar, over the Tademait Plateau (point A in Fig.8a), and between the Hoggar and the
 368 Tibesti (point B). However, only the wind west of the Hoggar is perturbed during these 3
 369 days, showing the preponderance of dynamical processes downwind of the Hoggar on vortex
 370 initiation. One day before initiation, a significant relative vorticity anomaly extends the
 371 average vorticity strip (Fig.5b) in the lee of the Hoggar (Fig.8d). The vortex is then
 372 asymmetric with maximum vorticity and wind anomalies north of the vortex center (point C
 373 in Fig.8b). The northeast side of the vortex is alimented by an easterly flow deviated around
 374 the southern edge of the Hoggar mountain (point D). The next day, the center of the vortex

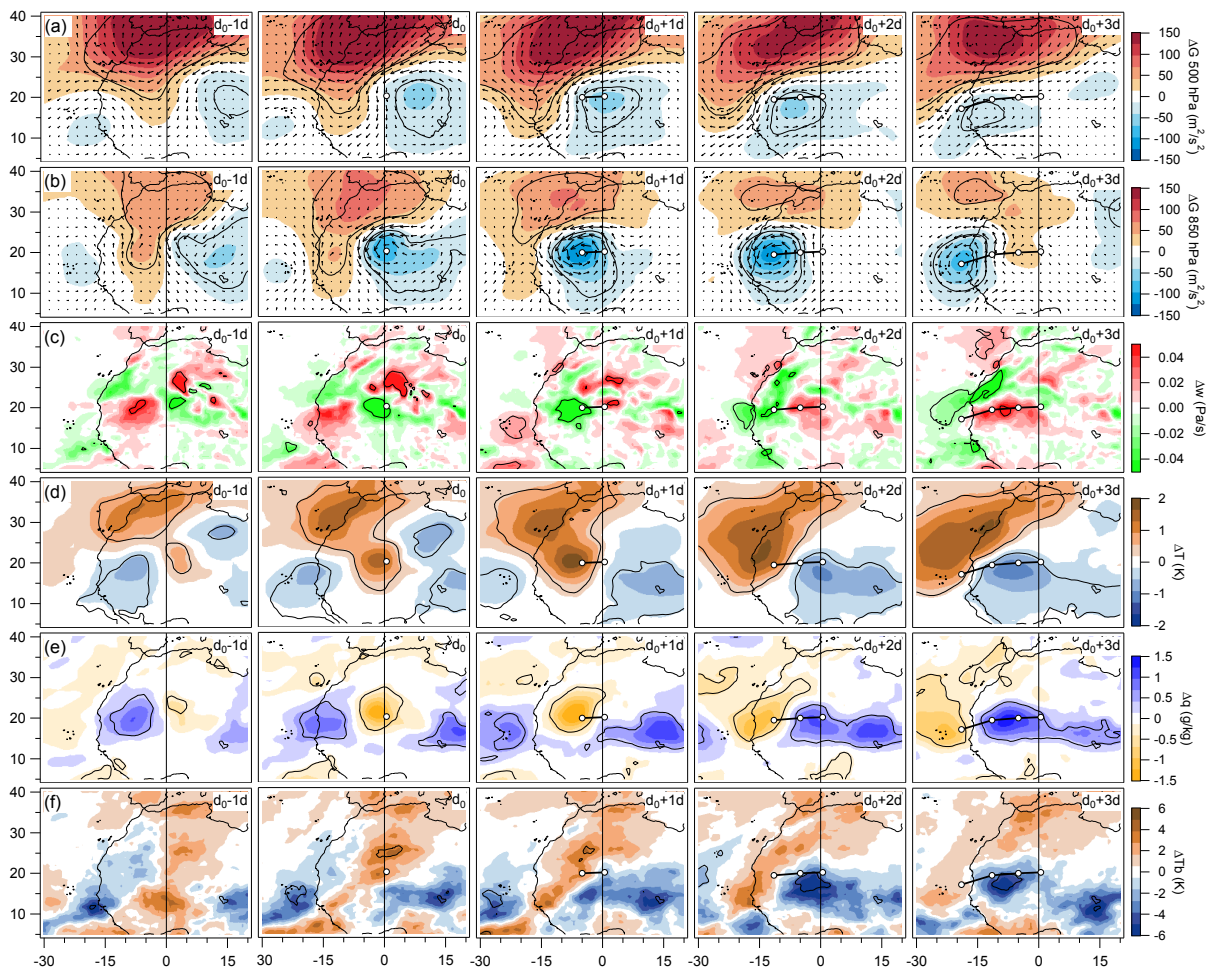
375 (point F in Fig. 8c) is located about 6° further west, giving a speed of about 7.7 ms^{-1} that
376 corresponds to the north-east wind speed to its north. The southwesterly monsoon flow (point
377 E in Fig.8c) is reinforced and recurves to form the eastern side of the vortex which is then
378 more axisymmetric.

379 The dynamical perturbation due to the mountain is complex and involves different
380 processes that may lead to the formation of vortices downwind. As discussed in Mozer and
381 Zehnder (1996a and b) (hereinafter MZa and MZb), the conservation of the potential vorticity
382 for a dry flow passing south of an isolated mountain (without column depth change) may
383 result in a low-level jet that is barotropically unstable, leading to the production of synoptic
384 vortices that separate from the mountains and move downstream. However, the jet south of
385 the Hoggar (point D) is weak here and the Hoggar vortex initiation seems more in agreement
386 with the vortex generated during the transient period at the beginning of the MZ simulations.
387 This transient period is associated with the formation of a so-called starting vortex attributed
388 to column stretching as the air initially at the top of the mountain is forced downstream
389 (Huppert and Brian 1976). In MZ simulations, the transient period results from the
390 instantaneous incorporation of orography in the flow, but it could result here from the rapid
391 intensification of the easterly flow over the mountain. A starting vortex indeed also appears
392 for wind modulations due to planetary Rossby waves in an easterly flow over orography
393 (Zehnder 1991). The evolution shown in figures 7 and 8 resembles the Zehnder results with a
394 cyclonic vortex forming in the lee of the mountain while a wave trough is still quite far to the
395 east, displaced southward (as point E in Fig.7c) and reinforced because of the conservation of
396 the total vorticity. The fact that the vortex appears while the easterly flow is reinforced by the
397 “Gibraltar high” and the approaching trough suggests that Hoggar vortex initiation process
398 could be understood more as a starting vortex rather than a vortex due to barotropic
399 instability of the jet south of the Hoggar. Nevertheless, such barotropic and baroclinic
400 instabilities due to the strong cyclonic shear existing between the Greenwich meridian and
401 the coast certainly plays a role in intensifying and maintaining the vortex, this is analyzed in
402 the next section.

403 **5. Hoggar vortex evolution**

404 After its initiation, the vortex moves westward along 20°N and reaches a maximum
405 strength around 10°W . The “Gibraltar high” remains quite stationary between d_0-1d and
406 d_0+3d and provides strong easterly winds on the north side of the vortex during its genesis

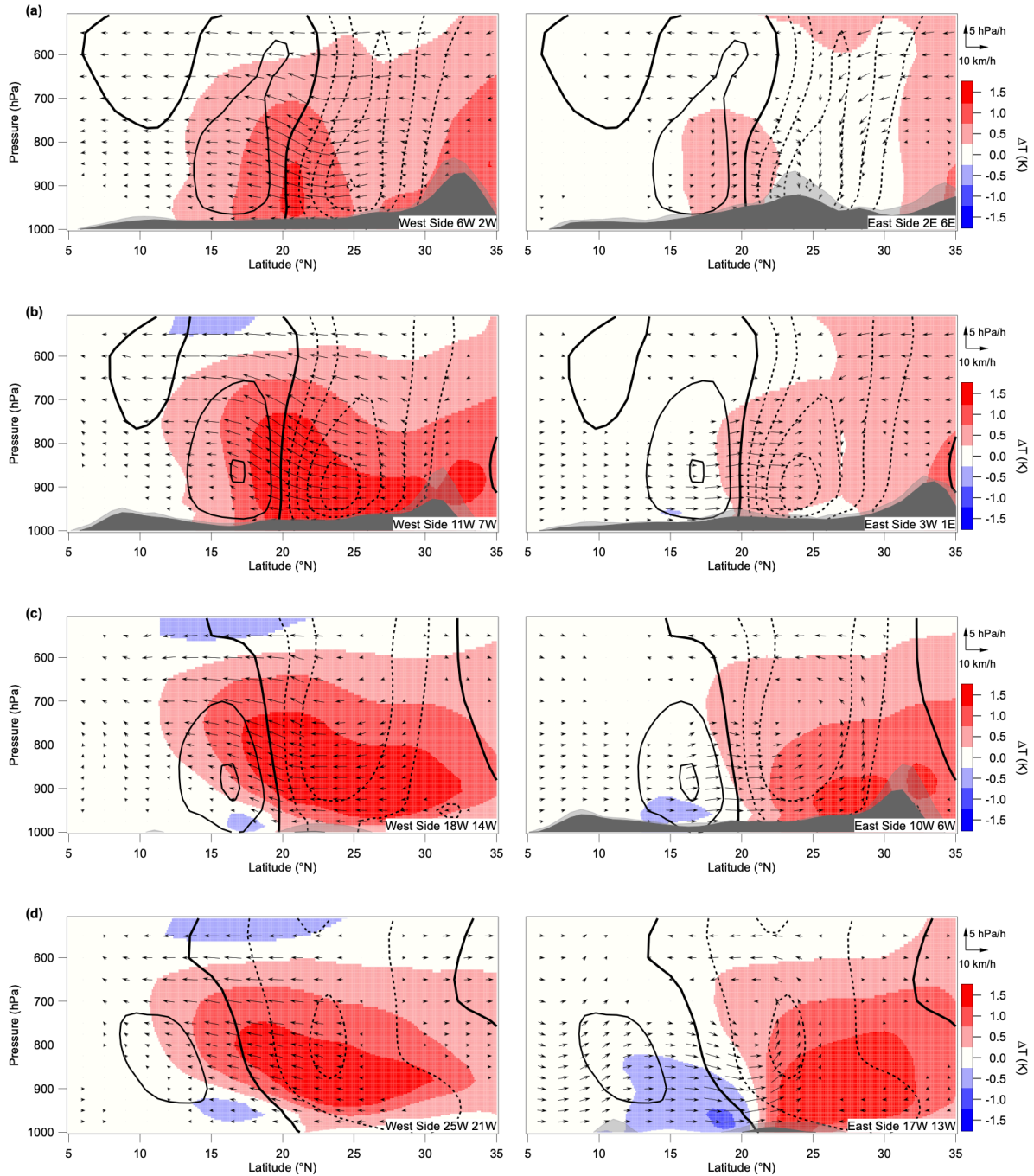
407 and during its progression toward the coast (Fig.9a and 9b). Between d_0-1d and d_0+1d , these
 408 easterly winds are associated with a significant subsidence anomaly (Fig.9c) above the
 409 Hoggar associated with warm (Fig.9d) and dry (Fig.9a) anomalies in the vortex. These dry
 410 processes during the vortex genesis are consistent with the band of positive T_b anomaly
 411 measured from space east of the Greenwich meridian at d_0-1d (Fig. 9f) and associated with a
 412 northerly wind anomaly. The positive T_b anomaly is large and significant near $25^\circ N$ at d_0 and
 413 consistent with subsiding warm and dry air north and west of the vortex center. During the
 414 vortex progression over the continent, warm and dry Saharan air is advected southward in the
 415 west side of the vortex. The resulting warm anomaly near the center of the vortex (Fig. 9d)
 416 gives a low-level warm-core structure that decreases the vortex cyclonic circulation above
 417 and confines the vortex circulation at low-levels.



418
 419 Figure 9: As in figure 7, but for the period [d_0-1 , d_0+3 days] for the anomaly of different dynamical and
 420 thermodynamical parameters from top to bottom: (a) geopotential height ΔG at 500hPa and (b) 850 hPa, (c)
 421 vertical velocity $\Delta\omega$ (positive downward), (d) temperature ΔT and (e) specific humidity Δq at 850 hPa, and (f)
 422 infrared window brightness temperature ΔT_b measured by the geosynchronous satellite Meteosat. The white
 423 markers represent the evolution of the position of the dynamical center of the 850 hPa vortex from d_0 .

424 On the other hand, the warm anomaly over the Atlantic Ocean West of Morocco tends to
425 maintain the anticyclonic geostrophic circulation around the “Gibraltar high” at 500 hPa (Fig.
426 9a). When the vortex reaches the coast, there is a large band of warm and dry anomaly over
427 the ocean and a band of cold and moist anomaly over the Sahelian zone between 15°N and
428 20°N. This evolution of the low-level temperature and humidity (Fig. 9d and 9e) is consistent
429 with the evolution of the observed anomaly of infrared brightness temperature (Fig. 9f). In
430 particular, negative T_b anomalies, which correspond to enhanced mid and high cloud cover
431 computed using thresholds at 230K and 210K (not shown) are associated with colder and
432 moister air temperature at low-levels, especially at d_0+2d and d_0+3d . At this time, the high
433 cloud cover north of 15°N is maximal in the east side of the vortex that is equivalent to the
434 southerly wind sector of an AEW-N. This is in agreement with previous studies (see e.g.,
435 Duvel 1990, Gu et al. 2004, Kiladis et al. 2006) showing maximum convection in the
436 southerly wind sector of the wave north of 15°N. This is in contrast with the maximum
437 convection and mesoscale convective systems found in the wave trough around 10°N for
438 AEW-S between the Greenwich meridian and the coast (see e.g., Kiladis et al. 2006, Núñez
439 Ocasio et al. 2020). This moist anomaly over Sahelian regions is probably similar to the
440 moisture surges discussed in detail in Couvreur et al. (2009) for June 2006 and to the
441 northward burst of the West African monsoon studied in Cuesta et al. (2009) for the end of
442 July 2006. On the opposite, the west side of the vortex with positive T_b anomalies indicates a
443 region of suppressed convection ahead of the vortex due to dry and warm northerlies. As
444 stated in section 2, some of these dry vortices can lead to cyclogenesis, either near the coast
445 or later over the Atlantic (e.g. Chen et al. 2008, Chen and Liu 2014, Duvel 2021). They are
446 however poorly cyclogenetic compared with vortices of the AEW-S partly because they tend
447 to occur before the heart of the hurricane season, but also, as stated by Hopsch et al. (2010),
448 because warm and dry conditions west of the AEW trough, caused by advection of Saharan
449 air, inhibit the development of deep convection and further deepening of the wave trough.

450 Figure 10 shows the evolution of the anomalies of the three-dimensional dynamical
451 structure of the vortex as it moves toward the coast. At d_0 , the vortex is strongly asymmetric
452 with an easterly wind anomaly of 4 m s^{-1} at 25°N and a westerly wind anomaly of only
453 1.5 m s^{-1} at 17°N (Fig. 11a). The southerly wind perturbation on its east side is weak and
454 vanishes above 800 hPa. This strong asymmetry of the wind anomaly is consistent with the
455 transient period discussed above and suggests that the main driving force of the vortex
456 formation at this early stage is the acceleration of the northeasterlies near the surface



457
 458 Figure 10: July and August latitudinal distribution of the anomaly of the temperature profiles (colors) and
 459 meridional and vertical wind (arrows) averaged over the west side (left) and the east side (right) of the
 460 composite vortex for (a) d_0 , (b) d_0+1 day, (c) d_0+2 days, and (d) d_0+3 days. The longitudes
 461 defining the west and east sides are indicated on the lower right corner of each panel. The corresponding
 462 zonal wind anomalies (contours, $\Delta u = \pm 1 \text{ ms}^{-1}$ starting from 0 with bold contour) is averaged for the central part
 463 of the vortex located between the west and east sides. The average (dark grey) and the maximum (light grey)
 464 orography for the west and the east side of the vortex are also displayed.

465 northwest of the Hoggar. The associated perturbation of northeasterly and subsiding winds up
 466 to 500 hPa is consistent with a reinforcement of the Libyan high circulation associated with
 467 the “Gibraltar high” anomaly. A warming of more than 1K extends roughly between the

468 surface and 700 hPa on the west side of the vortex (Fig.10a) and certainly contributes to the
469 deepening of the vortex depression for the following day.

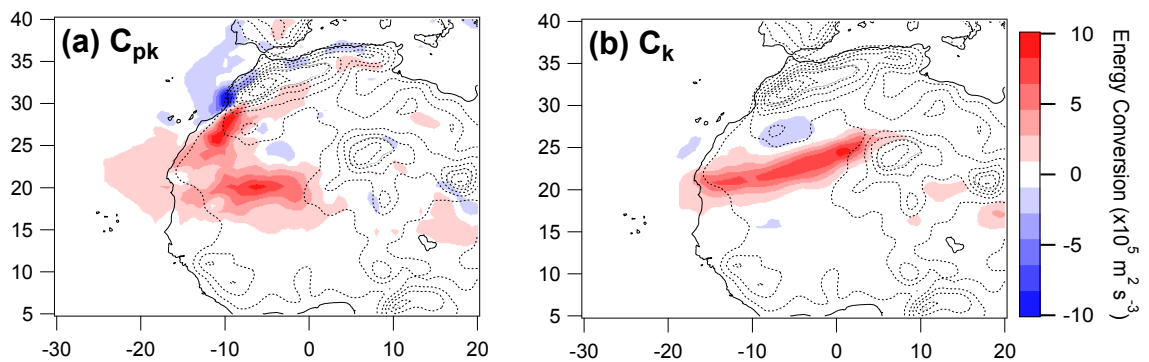
470 At d_0+1 day around 5°W (Fig.10b), the vortex is more axisymmetric and stronger with larger
471 warming on the west side for air rising over the monsoon flow. On the east side, a colder and
472 moister southerly wind perturbation penetrates further north. At d_0+2 days around 12°W
473 (Fig.10c), the vortex is shifted upward with maximum easterlies around 800 hPa on the north
474 side. On the west side, the warming is maximal around 800 hPa at 15°N and located above a
475 cold anomaly at the surface. Both the northerly wind uplift on the west side and the southerly
476 wind uplift on the east side (Fig.9c and 10c) participate in the vortex uplift. This tendency is
477 reinforced at d_0+3 days (Fig.10d) with wind perturbations maximal around 800 hPa at 19°W .
478 This vortex ascent during its travel between the Hoggar and the coast may be attributed to the
479 lift of the Saharan air above the monsoon flow on its west side and to the lift possibly related
480 to orography on its east side after d_0+2 days. This is consistent with the lifting process
481 analyzed by Drame et al. (2011) for a Saharan Air Layer (SAL) episode that occurred in July
482 2010 in association with a westward moving thermal low that is indeed one of the 166
483 Hoggar vortices considered here.

484 An exhaustive computation of the energy budget of the vortices is outside the scope of
485 this study. However, two important kinetic energy conversion parameters may be estimated
486 on the basis of the composite perturbations in order to estimate the consistency with the
487 energy budget of AEW-N at low-level. Previous results on AEWs (e.g., Norquist et al. 1977,
488 Lau and Lau 1992, Diedhiou et al. 2002, Alaka and Maloney 2014, Hamilton et al. 2020,
489 White et al. 2021) found large positive values of the baroclinic overturning term and of the
490 barotropic conversion term at low levels around 20°N and west of the Hoggar. These terms
491 represent respectively the conversion of eddy available potential energy to eddy kinetic
492 energy (C_{pk}) and the transfer of mean to eddy kinetic energy (C_k) and are defined as:

493
$$C_{pk} = -\frac{R}{P} \overline{\omega' T'} ; \quad C_k = -\overline{[\mathbf{V}'_H \cdot (\mathbf{V}' \cdot \nabla) \mathbf{V}'_H]}$$

494 where \mathbf{V} is the three-dimensional wind, \mathbf{V}_H is horizontal wind (m s^{-1}), ω is pressure velocity
495 (Pa s^{-1}), T is air temperature (K). The prime is used to represents composite anomalies (i.e.,
496 eddy perturbations) and the overbar represents an average between d_0-4 days and d_0+3 days.
497 As expected, the warm northerly wind anomaly rising on the west side of the vortex and the
498 cold southerly wind anomaly subsiding on the east side of the vortex (Fig.9c and 9d) give a

499 large positive C_{pk} at low-levels around 20°N between the Hoggar and the coast (Fig.11a) in
 500 agreement with previous results on AEW-N. There is also large C_{pk} south of the Atlas
 501 Mountains, due to rising warm air in the north side of the vortex (Fig.10c and 10d). However,
 502 the nearly null C_{pk} near the Hoggar shows that baroclinic energy conversion plays no role in
 503 vortex genesis. Figure 11b shows large positive barotropic conversion C_k due to the large
 504 average cyclonic shear and the asymmetry of the vortex dominated by the northeasterly
 505 winds. This suggests that the kinetic energy of the vortex during its genesis and for its
 506 progression comes mainly from the mean northeasterly winds accelerated by the "Gibraltar
 507 High". This large C_k at low-level is also in agreement in location and amplitude with previous
 508 studies on AEW-N.



509
 510 Figure 11: (a) baroclinic overturning (C_{pk}) and (b) barotropic energy conversion (C_k) between d_0-4 days and
 511 d_0+3 days at 900hPa.

512 6. Summary and discussion

513 Most of the low-level synoptic vortices formed over West Africa and propagating to the
 514 Atlantic Ocean (i.e., Atlantic vortices) on the AEW-N track are initiated downwind of the
 515 Hoggar Mountains in July and August. The main specificity in the local circulation for these
 516 months compared to June and September is the reinforcement of the low-level easterly winds
 517 over the Hoggar and the vertical expansion of subsiding easterly winds up to 400 hPa. This
 518 vertical expansion favors the development of a low-level easterly jet that may be hampered in
 519 June and September due to westerly winds above 800 hPa. The reinforcement and the larger
 520 vertical expansion of these easterlies in July and August are associated with the northward
 521 migration of the SHL. At the synoptic time-scales, the vortex initiation is associated with an
 522 additional strengthening of these easterlies over the Hoggar. This extra strengthening is
 523 associated with a high-pressure anomaly that develops first at mid-level around the Strait of
 524 Gibraltar three days before Hoggar vortex initiations and then extends downward. Locally,

525 this "Gibraltar high" anomaly corresponds to an amplification of the Libyan anticyclone
526 which is also a characteristic of July. Hoggar vortex initiations are also statistically associated
527 with a depression coming from the east and located at around 30°E at d₀-3 days. This
528 "easterly low" appears first at low-level and then strengthens and extends up to 500 hPa
529 before Hoggar vortex initiation. The precise origin of the "Gibraltar high" anomaly is
530 probably multifactorial and deserves further studies. It could be related in particular to the
531 SHL intraseasonal variability mode studied by Chauvin et al. (2010). This mode is linked to
532 polar and subtropical jet fluctuations over the North Atlantic with a characteristic time scale
533 of about 15 days and has some resemblance with the persistent mid-level wind anomaly
534 around the "Gibraltar high".

535 The composite analysis thus objectively reveals that Hoggar vortices are statistically
536 associated with the evolution of two features, the "Gibraltar high" and an "easterly low", both
537 of which appear more than three days before vortex initiation. However, this composite
538 initiation scenario being statistical, Hoggar vortices are certainly developing with various
539 combination of these two features that are basically disconnected. The "Gibraltar high"
540 indeed evolves over a much longer time-scale, as shown by its persistence in Figures 7 and 9,
541 compared to the more frequent and faster "easterly low". The wave pattern evident in Figure
542 7, especially in Figure 7c at d₀-2 days, suggests that the "easterly low" statistically
543 corresponds to the eastern trough of an initially weak easterly wave. The "Gibraltar high"
544 clearly extends southward and downward as the ridge of this wave crosses the Greenwich
545 meridian. Statistically, the Hoggar vortex initiation correspond therefore to an intensification
546 of this easterly wave by the formation of an orographic vortex while transient northeasterly
547 winds blow over the Hoggar between this reinforced ridge and the eastern trough. As
548 suggested in figure 11b, the source of intensification of this vortex could be mostly kinetic
549 energy transfer from the persistent northeasterly flow provided by the southward and
550 downward extension of the "Gibraltar high" perturbation.

551 An important point is that both features lead to reinforced northeasterly wind over the
552 Hoggar before vortex initiation southwest of the Hoggar about 1000 km east of the center of
553 the "easterly low". The flow pattern around the Hoggar near initiation time shows some
554 analogy with the transient period in the simulations analyzed in MZa, MZb and Zehnder
555 (1991) which leads to a so-called starting vortex attributed to column stretching as the air
556 initially at the top of the mountain is forced downstream. For the observed Hoggar vortices,

557 the transient character could result from the rapid intensification of the easterly flow due to
558 the Gibraltar high development. One day before vortex initiation, the reinforcement of the
559 northeasterly flow northwest of the Hoggar leads to a cyclonic vorticity anomaly in the lee of
560 the mountain. The vortex then amplifies asymmetrically with a reinforcement of the wind and
561 of the cyclonic vorticity north of its center and becomes afterward more symmetric with an
562 amplification of the monsoon flow on its south side. The present analysis is concerned mostly
563 with the origin of the vortices and their impact on the AEW-N amplitude. As might be
564 expected, the vortex characteristics after their initiation resemble those of the AEW-N
565 reported in the literature since the pioneering work of Carlson (1969) and Burpee (1972).
566 Among the 166 Hoggar vortices, there are about 20% which are following a previous one and
567 forming therefore a sort of wave packet of larger amplitude. In the composite Hoggar vortices
568 shown in Figures 7 and 9, the trough which forms statistically near 30°E at d₀-3d is located at
569 approximately 35° east of the previous vortex (Fig.7c) and takes about 4-5 days to reach the
570 position of this previous vortex, which is within the typically observed wavelength and period
571 of AEWs. The maintenance of this vortex up to the coast may be attributed to low-level
572 barotropic and baroclinic energy conversions resulting mostly from the strong cyclonic shear
573 between the northeasterlies and the monsoon flow, in agreement with previous studies on
574 AEW-N.

575 The two paths of the AEWs are well known, but they are often considered as the
576 expression of the same phenomenon having its origin in the instability of the AEJ. For
577 example, in Kiladis et al. (2006) and Hall et al. (2006), differences in the nature of AEWs are
578 mostly attributed to differences in the basic-state AEJ depending in particular on the season.
579 Hall et al. (2006) also highlight the fact that the modal growth in a dry model is not sufficient
580 to account for the presence of AEWs and that a triggering of the wave is necessary. This
581 triggering is generally attributed to convective warming in the heart or at the root of the AEJ
582 (see e.g., Thorncroft et al. 2008). It is interesting to note that Thorncroft et al (2008) found
583 that the maximum triggering efficiency is obtained for a shallow convective warming at
584 20°N-15°E, that is the statistical position of approaching trough one day before initiation
585 (Fig.7c). While the model used in Thorncroft et al. (2008) has no orography, it still has the
586 temperature structure of the SHL and the associated large-scale barotropic and baroclinic
587 instabilities. As shown in previous studies (see e.g., Grogan et al. 2016, Nathan et al. 2017),
588 this triggering could also be due to the warming resulting from the radiative forcing of
589 Saharan mineral dust. The role of mid-latitudes in triggering AEWs has also been highlighted

590 in Leroux et al. (2011) who showed using an idealized model that AEW packets can be
591 associated with a slow eastward moving high pressure over the North Atlantic that presents
592 similitudes with the “Gibraltar high” and with the perturbations at the origin of the SHL
593 variability in Chauvin et al. (2010).

594 The results presented above offer another possibility for the triggering or intensification
595 of AEW-N by invoking the impact of orographic disturbances caused by enhanced easterly
596 winds over the Hoggar. This assumption does not contradict that of White et al (2021) who
597 attribute the marked decrease in AEW-N energy in a model where the Hoggar and Tibesti
598 mountains have been removed to the reduction in baroclinic energy conversion due to
599 reduced vertical wind shear. This weaker vertical shear results from enhanced low-level
600 easterlies to the west of the Hoggar and to a weaker AEJ due to reduced meridional surface
601 temperature gradient (see also Hamilton et al. 2017). In fact, both processes may explain the
602 high sensitivity of the AEW-N amplitude to the removing of the Hoggar and Tibesti
603 orography in the White et al. (2021) sensitivity test. The “vertical shear hypothesis” considers
604 that reinforced easterlies west of the flattened Hoggar region inhibit AEW-N, while the
605 "orographic perturbation hypothesis” considers that reinforced easterlies over the orography
606 is a source of intensification of AEW-N. To test more specifically the "orographic
607 perturbation hypothesis” proposed here, additional sensitivity tests could be performed by
608 varying the intensity and the vertical profile of the wind over the Hoggar orography, for
609 example by imposing different latitudinal positions of the SHL.

610

611 *Acknowledgments*

612 I thank Nick Hall, François Lott, Hugo Bellenger and three reviewers for reading the
613 manuscript and for making helpful comments and suggestions. ECMWF ERA-Interim data
614 used in this study have been obtained from the ECMWF data server and processed on the
615 IPSL mesocenter ESPRI facility which is supported by CNRS, UPMC, Labex L-IPSL, CNES
616 and Ecole Polytechnique.

617 *Data Availability Statement*

618 ERA-Interim data used in this study are openly available at <https://www.ecmwf.int/>.

619

620

621

622

REFERENCES

623

Abdou, K., D. J. Parker, B. Brooks, N. Kalthoff and T. Lebel, 2010: The diurnal cycle of lower boundary-layer wind in the West African monsoon, *Q. J. Roy. Meteor. Soc.*, **136**, 66–76.

626

Alaka, G. J., and E. D. Maloney, 2014: The intraseasonal variability of African easterly wave energetics. *J. Climate*, **27**, 6559–6580.

628

Berry, G., and C. D. Thorncroft, 2005: Case study of an intense African easterly wave. *Mon. Wea. Rev.*, **133**, 752–766.

630

Bou Karam, D., C. Flamant, P. Tulet, M. C. Todd, J. Pelon, and E. Williams, 2009: Dry cyclogenesis and dust mobilization in the intertropical discontinuity of the West African Monsoon: A case study, *J. Geophys. Res.*, **114**, D05115.

633

Burpee, R. W., 1972: The origin and structure of easterly waves in the lower troposphere of North Africa. *J. Atmos. Sci.*, **29**, 77–90.

635

Carlson, T. N., 1969: Synoptic histories of three African disturbances that developed into Atlantic hurricanes. *Mon. Wea. Rev.*, **97**, 256–276.

637

Chauvin, F., R. Roehrig, and J.-P. Lafore, 2010: Intraseasonal variability of the Saharan heat low and its link with midlatitudes. *J. Climate*, **23**, 2544–2561.

639

Chen, S.-H., and Y.-C. Liu, 2014: The relation between dry vortex merger and tropical cyclone genesis over the Atlantic Ocean. *J. Geophys. Res. Atmos.*, **119**, 11 641–11 661.

641

Chen T. C., S-Y. Wang, and A. J. Clark, 2008. North Atlantic hurricanes contributed by African easterly waves north and south of the African easterly jet. *J. Climate*, **21**, 6767–6776.

644

Cook, K. H., 1999: Generation of the African easterly jet and its role in determining West African precipitation. *J. Climate*, **12**, 1165–1184.

646

Couvreux, F., F. Guichard, O. Bock, B. Campistron, J.-P. Lafore, and J.-L. Redelsperger, 2010: Synoptic variability of the monsoon flux over West Africa prior to the onset. *Quart. J. Roy. Meteor. Soc.*, **136**, 159–173

648

649 Cuesta J, C. Lavaysee, C. Flamant, M. Mimouni, and P. Knippertz, 2009. Northward burst of
650 the West African monsoon leading to rainfall over the Hoggar Massif, Algeria. *Q. J. R.*
651 *Meteorol. Soc.* **135**: 34–42.

652 Dee, D.P., and co-authors, 2011: The ERA-Interim reanalysis: Configuration and
653 performance of the data assimilation system. *Quart. J. Roy. Meteor. Soc.*, **137**, 553–597.

654 Diedhiou, A., Janicot, S., Viltard, A., and P. de Felice, 2002: Energetics of easterly wave
655 disturbances over West Africa and the tropical Atlantic: A climatology from 1979-95
656 NCEP/NCAR reanalyses. *Climate Dynamics*, **18**, 487–500.

657 Drame, M., G. S. Jenkins, M. Camara, and M. Robjhon, 2011: Observations and simulation
658 of a Saharan air layer event with a midtropospheric dust layer at Dakar, Senegal, 6–7 July
659 2010. *J. Geophys. Res.*, **116**, D21204.

660 Duvel, J. P., 1990: Convection over tropical Africa and Atlantic Ocean during Northern
661 summer. Part II: Modulation by easterly waves. *Mon. Wea. Rev.*, **118**, 1855-1868.

662 Duvel, J. P., 2015: Initiation and Intensification of Tropical Depressions over the Southern
663 Indian Ocean: Influence of the MJO. *Mon. Wea. Rev.*, **143**, 2170–2191.

664 Duvel, J. P., S.J. Camargo and A.H. Sobel, 2017: Role of the Convection Scheme in
665 Modeling Initiation and Intensification of Tropical Depressions over the North Atlantic.
666 *Mon. Wea. Rev.*, **145**, 1495-1509.

667 Duvel, J. P., 2021: On vortices initiated over West Africa and their impact on North Atlantic
668 tropical cyclones. *Mon. Wea. Rev.*, **149**, 585-601.

669 Fiedler, S., K. Schepanski, P. Knippertz, B. Heinold, and I. Tegen, 2014: How important are
670 atmospheric depressions and mobile cyclones for emitting mineral dust aerosol in North
671 Africa?, *Atmos. Chem. Phys.*, **14**, 8983–9000.

672 Grogan, D. F. P., Nathan, T. R., and Chen, S. H.: Effects of Saharan Dust on the Linear
673 Dynamics of African Easterly Waves, *J. Atmos. Sci.*, **73**, 891911, 2016.

674 Gu, G., R. F. Adler, G. J. Huffman, and S. Curtis, 2004: African easterly waves and their
675 association with precipitation. *J. Geophys. Res.*, **109** .D04101,
676 doi:10.1029/2003JD003967.

677 Hall, N. M. J., G. N. Kiladis, and C. D. Thorncroft, 2006: Three-dimensional structure and
678 dynamics of African easterly waves. Part II: Dynamical modes. *J. Atmos. Sci.*, **63**(9),
679 2231–2245.

680 Hamilton, H. L., Núñez Ocasio, K. M., Evans, J. L., Young, G. S., and J. D. Fuentes, 2020:
681 Topographic influence on the African Easterly Jet and African Easterly Wave energetics.
682 *J. Geophys. Res.: Atmospheres*, **125**, e2019JD032138.

683 Hodges, K., D. Chappell, G. Robinson, and G. Yang, 2000: An improved algorithm for
684 generating global window brightness temperatures from multiple satellite infrared
685 imagery. *J. Atmos. Oceanic Technol.*, **17**, 1296–1312.

686 Hopsch S. B., C.D. Thorncroft, and K. Hodges, 2007: West African storm tracks and their
687 relationship to Atlantic tropical cyclones. *J. Climate* **20**: 2468 – 2483.

688 Hopsch, S. B., C. D. Thorncroft, and K. R. Tyle, 2010: Analysis of African easterly wave
689 structures and their role in influencing tropical cyclogenesis. *Mon. Wea. Rev.*, **138**, 1399–
690 1419.

691 Huppert, H. E., and K. Bryan, 1976: Topographically generated eddies. *Deep-Sea Res.*
692 *Oceanogr. Abstr.*, **23**, 655–679

693 Kiladis, G. N., C. D. Thorncroft, and N. M. J. Hall, 2006: Three-dimensional structure and
694 dynamics of African easterly waves. Part I: Observations. *J. Atmos. Sci.*, **63**, 2212–2230.

695 Knapp, K.R., M.C. Kruk, D.H. Levinson, H.J. Diamond, and C.J. Neumann, 2010: The
696 International Best Track Archive for Climate Stewardship (IBTrACS): Unifying tropical
697 cyclone data. *Bull. Amer. Meteor. Soc.*, **91**, 363–376.

698 Lau, K.-H., and N.-C. Lau, 1992: The energetics and propagation dynamics of tropical
699 summertime synoptic-scale disturbances. *Mon. Wea. Rev.*, **120**, 2523–2539.

700 Leroux, S., N. M. Hall, and G. N. Kiladis, 2011: Intermittent African Easterly Wave Activity
701 in a Dry Atmospheric Model: Influence of the Extratropics, *J. Climate*, **24**, 5378–5396.

702 Mekonnen, A., C. D. Thorncroft, and A. R. Aiyyer, 2006: Analysis of convection and its
703 association with African easterly waves. *J. Climate*, **19**, 5405–5421.

704 Mekonnen, A., and W. B. Rossow, 2018: The interaction between deep convection and
705 easterly wave activity over Africa: Convective transitions and mechanisms. *Mon. Wea.*
706 *Rev.*, **146**, 1945–1961.

707 Mozer, J. B., and J. A. Zehnder, 1996a: Lee vorticity production by large-scale tropical
708 mountain ranges. Part I: Eastern North Pacific tropical cyclogenesis. *J. Atmos. Sci.*, **53**,
709 521–538

710 Mozer, J. B., and J. A. Zehnder, 1996b: Lee vorticity production by large-scale tropical
711 mountain ranges. Part II: A Mechanism for the Production of African Waves. *J. Atmos.*
712 *Sci.*, **53**, 539–549.

713 Nathan, T. R., Grogan, D. F. P., and Chen, S.-H.: Subcritical Destabilization of African
714 Easterly Waves by Saharan Mineral Dust, *J. Atmos. Sci.*, **74**, 10391055, 2017.

715 Norquist, D. C., E. E. Recker, and R. J. Reed, 1977: The energetics of African wave
716 disturbances as observed during phase III of GATE. *Mon. Wea. Rev.*, **105**, 334–342.

717 Núñez Ocasio, K. M., J. L. Evans, and G. S. Young, 2020: A wave-relative framework
718 analysis of AEW–MCS interactions leading to tropical cyclogenesis. *Mon. Wea. Rev.*,
719 **148**, 4657–4671.

720 Parker, D., R. Burton, A. Diongue-Niang, R. Ellis, M. Felton, C. Taylor, C. Thorncroft, P.
721 Bessemoulin, and A. Tompkins, 2005: The diurnal cycle of the west African monsoon
722 circulation. *Q. J. R. Meteorol. Soc.*, **131**: 2839– 2860.

723 Pytharoulis, I., and C. D. Thorncroft, 1999: The low-level structure of African easterly waves
724 in 1995. *Mon. Wea. Rev.*, **127**, 2266–2280.

725 Reed, R. J., E. Klinker, and A. Hollingsworth, 1988: The structure and characteristics of
726 African easterly wave disturbances as determined from the ECMWF operational
727 analysis/forecast system. *Meteor. Atmos. Phys.*, **38**, 22–33.

728 Russell, J. O., A. Aiyyer, J. D. White, and W. Hannah, 2017: Revisiting the connection
729 between African easterly waves and Atlantic tropical cyclogenesis. *Geophys. Res. Lett.*,
730 **44**, 587–595, <https://doi.org/10.1002/2016GL071236>.

731 Rydbeck, A. V., and Maloney, E. D., 2014: Energetics of East Pacific easterly waves during
732 intraseasonal events. *Journal of Climate*, **27** , 7603–7621.

733 Sultan, B., and S. Janicot, 2003: The West African monsoon dynamics. Part II: The
734 “preonset” and “onset” of the summer monsoon. *J. Climate*, **16** , 3407–3427.

735 Thorncroft, C. D., and D. P. Rowell, 1998: Interannual variability of African wave activity in
736 a general circulation model. *Int. J. Climatol.*, **18**, 1305–1323.

- 737 Thorncroft, C. D., and M. Blackburn, 1999: Maintenance of the African easterly jet. *Quart. J.*
738 *Roy. Meteor. Soc.*, **125**, 763–786.
- 739 Thorncroft, C. D., and K. Hodges, 2001: African easterly wave variability and its relationship
740 to Atlantic tropical cyclone activity. *J. Climate*, **14**, 1166–1179.
- 741 Thorncroft, C. D., N. M. J. Hall, and G. N. Kiladis, 2008: Three-dimensional structure and
742 dynamics of African easterly waves. Part III: Genesis. *J. Atmos. Sci.*, **65**, 3596–3607.
- 743 White, J. D., A. Aiyyer and J.O. Russell, 2021: The Impact of Orography on the African
744 Easterly Wave Stormtrack. *J. Geophys. Res.: Atmospheres*, **126**, e2020JD033749.
- 745 Wu, M. C., O. Reale, S. D. Schubert, M. J. Suarez, R. D. Koster, and P. J. Pegion, 2009:
746 African easterly jet: structure and maintenance. *J. Climate*, **22**, 4459–4480.
- 747 Zehnder, J., 1991: The interaction of planetary-scale tropical easterly waves with topography:
748 A mechanism for the initiation of tropical cyclones. *J. Atmos. Sci.*, **48**, 1217–1230.